JOURNAL OF SPACECRAFT AND ROCKETS
Vol. 47, No. 3, May–June 2010

General Bang–Bang Control Method for Lorentz Augmented Orbits

Brett Streetman*
Draper Laboratory, Cambridge, Massachusetts 02139
and
Mason A. Peck†
Cornell University, Ithaca, New York 14853

DOI: 10.2514/1.45704

An orbital control framework is developed for the Lorentz augmented orbit. A spacecraft carrying an electrostatic charge moves through the geomagnetic field. The resulting Lorentz force is used in the general control framework to evolve the spacecraft's orbit. The controller operates with a high degree and order spherical-harmonic magnetic field model by partitioning the space of latitude in a meaningful way. The partitioning reduces the complexity of the problem to a manageable level. A successful maneuver developed within this bang-off control framework results in a combined orbital plane change and orbit raising. The cost of this maneuver is in electrical power. Reductions in the power usage, at the expense of longer maneuver times, are obtained by using information about local plasma density.

Nomenclature

a	=	semimajor axis, m
$\mathbf{B}$	=	Earth's magnetic field, T
C	=	capacitance, F
E	=	specific energy, m/s
e	=	eccentricity
F_L	=	Lorentz force, N
h	=	specific angular momentum magnitude, m^2/s
$\mathbf{h}$	=	specific angular momentum, m^2/s
i	=	inclination, rad
L	=	length of cylindrical capacitor, m
$\hat{\mathbf{n}}$	=	Earth spin axis
n_e	=	electron number density, $1/m^3$
q	=	net spacecraft charge, C
q/m	=	charge-to-mass ratio, C/kg
R	=	stocking radius, m
r	=	radial coordinate, rad
$\mathbf{r}$	=	spacecraft position, m
r_s	=	wire sheath radius, m
u	=	argument of latitude, rad
$\mathbf{v}$	=	spacecraft velocity, m/s
ϵ_0	=	permittivity of free space, F/m
θ	=	azimuth angle, rad
μ	=	gravitational parameter, m^3/s^2
ν	=	true anomaly, rad
ϕ	=	colatitude, rad
Ω	=	spacecraft right ascension of the ascending node, rad
ω	=	argument of perigee, rad
ω_E	=	Earth's spin rate, rad/s

I. Introduction

PROPELLANTLESS propulsion opens up new possibilities for spacecraft missions. One form of propellantless propulsion is the Lorentz augmented orbit (LAO), which was first presented by Peck [1], and further examined through our later work [2,3]. A body with net charge q moving in a magnetic field $\mathbf{B}$ experiences a Lorentz force

$$\mathbf{F}_L = q(\mathbf{v} - \omega_E \hat{\mathbf{n}} \times \mathbf{r}) \times \mathbf{B} \tag{1}$$

where $\mathbf{r}$ is measured in an Earth-centered, inertial reference frame. The velocity correction $(-\omega_E \hat{\mathbf{n}} \times \mathbf{r})$ is required because the magnetic field $\mathbf{B}$ is constant only in an Earth-fixed frame. The charge-to-mass ratio q/m of the spacecraft determines the magnitude of the Lorentz acceleration. The direction of this acceleration is fixed by the velocity of the spacecraft and the magnetic field at the spacecraft location. Because the charge on the spacecraft can be maintained solely with electrical power and because the Lorentz force acts externally, LAO technology represents propellantless propulsion. If q/m is varied as a control input, an LAO can achieve novel orbits and enable new missions.

Orbit perturbations on charged particles due to the Lorentz force have been observed in nature. Schaffer and Burns [4,5] and Hamilton [6] have studied these effects and derived various perturbation equations. They have shown that the Lorentz force acting on micron-sized, naturally charged dust grains creates significant changes in their orbits. This effect explains features seen in the ethereal rings of Jupiter. The dynamics of these charged dust grains is well understood in the context of naturally occurring systems.

Perturbations have also been examined in the context of the natural charging of Earth-based spacecraft. Early studies include Sehnal [7] in 1969. Others have tried to explain orbital deviations of the LAGEOS spacecraft using naturally occurring Lorentz forces, including work by Vokrouhlicky [8] and later Abdel-Aziz [9]. In this work, we wish to not only examine the perturbations caused by the Lorentz force, but to expand the available orbits and add controlled charging to exploit the Lorentz dynamics for engineering applications through LAOs.

Many other propellantless propulsion systems have been proposed. The electrodynamic tether system is closely related to LAO. Tethers force current through a long conductor [10]. The current in this tether moving with the satellite creates a Lorentz force. By using a current in a wire rather than a space charge on the spacecraft, a tether can produce forces in directions an LAO spacecraft cannot. However, the direction of the tether must be controlled, whereas LAO is attitude independent. LAO and tethers (along with other propellantless propulsion systems) differ in from where they harvest energy. LAO does work on a satellite by using the rotation of Earth's magnetic field. If in a perfect vacuum, an LAO system would require only enough power to charged up and discharge the spacecraft. A tether system is essentially a device for converting between

Received 28 May 2009; revision received 21 August 2009; accepted for publication 27 August 2009.

*Senior Member Technical Staff, 555 Technology Square.
†Assistant Professor, Department of Mechanical and Aerospace Engineering, 212 Upson Hall. Member AIAA.

electrical energy and kinetic energy. Solar sails and magnetic sails harvest energy from the sun to perform propellantless maneuvers.

In addition to LAO, a charged spacecraft architecture has been proposed for formation flight [11,12]. The Coulomb Spacecraft Formation (CSF) concept makes use of the coulomb force acting between two charged satellites, rather than the Lorentz force. Whereas LAO uses an external force, CSF can produce only forces internal to the formation. The CSF system performs better at higher altitudes like geosynchronous earth orbit, whereas LAO produces more useful formation forces in low Earth orbit (LEO) [13].

Our earlier studies [1–3] present the dynamics of LAOs under simplified conditions, including greatly simplified magnetic field models. This study expands that analysis to include spherical-harmonic magnetic fields of arbitrary complexity. Section II gives an overview of the effect of the Lorentz force on an orbit, drawn from previous work. Section III discusses the general properties of the geomagnetic field. Section IV gives new material on possible LAO system architectures. Section V provides a discussion of the maneuver limitations introduced by the Lorentz force is presented, along with a compelling mission enabled by the LAO concept. Section VI considers the effects of ionospheric conditions on performance and power usage of an LAO spacecraft.

II. Lorentz Perturbations

The effects of the Lorentz force on an orbit are studied using perturbation methods. We have previously shown that the change in orbital energy E of a charged spacecraft affected by an arbitrary magnetic field is given by [2]

$$\dot{E} = \frac{q}{m}\omega_E[(\mathbf{v}\cdot\hat{\mathbf{n}})(\mathbf{B}\cdot\mathbf{r}) - (\mathbf{v}\cdot\mathbf{r})(\hat{\mathbf{n}}\cdot\mathbf{B})] \tag{2}$$

To describe this position $\mathbf{r}$ and velocity $\mathbf{v}$, we use an Earth-centered, inertial reference frame with spherical coordinates: radius r, colatitude ϕ, and azimuth angle θ, as shown in Fig. 1. In these coordinates, Eq. (2) can be expressed as

$$\dot{E} = \frac{q}{m}\omega_E[(r\mathbf{v}\cdot\hat{\mathbf{n}} - \cos\phi\mathbf{r}\cdot\mathbf{v})(\mathbf{B}\cdot\hat{\mathbf{r}}) + \sin\phi(\mathbf{r}\cdot\mathbf{v})(\mathbf{B}\cdot\hat{\phi})] \tag{3}$$

The $\hat{\mathbf{r}}$ and $\hat{\phi}$ unit vectors are shown in Fig. 1.

Change in vector angular momentum is also found from perturbation methods [2]:

$$\dot{\mathbf{h}} = \frac{q}{m}(\mathbf{B}\cdot\mathbf{r})\mathbf{v} - \frac{q}{m}(\mathbf{r}\cdot\mathbf{v})\mathbf{B} - \frac{q}{m}\omega_E(\mathbf{B}\cdot\mathbf{r})(\hat{\mathbf{n}}\times\mathbf{r}) \tag{4}$$

Equations (2) and (4) are used to obtain the derivatives of other orbital elements. Equation (4) leads to an expression for the derivative of inclination i [14]:

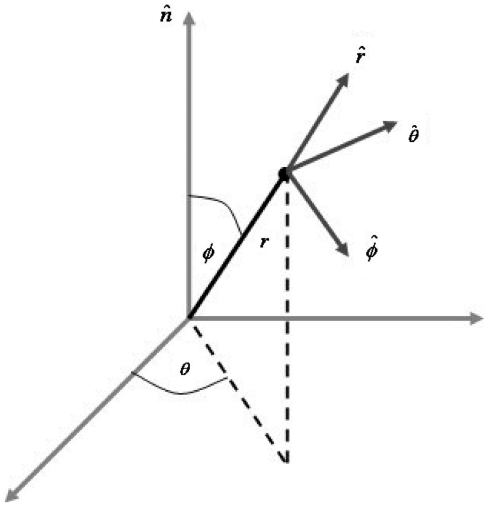

Fig. 1 Spherical coordinates and unit vectors used.

$$\frac{\mathrm{d}i}{\mathrm{d}t} = \frac{\dot{h}\cos i - \dot{\mathbf{h}}\cdot\hat{\mathbf{n}}}{h\sin i} \tag{5}$$

In the spherical coordinates, Eq. (5) becomes

$$\frac{\mathrm{d}i}{\mathrm{d}t} = \frac{-1}{h\omega_E\sin i}\dot{E} + \frac{q}{m}\frac{\cos i}{h^2\sin i}\left[\omega_E r^2(r\mathbf{v}\cdot\hat{\mathbf{n}} - \cos\phi\mathbf{r}\cdot\mathbf{v})(\mathbf{B}\cdot\hat{\mathbf{r}}) + \frac{h\cos i}{\sin\phi}(\mathbf{r}\cdot\mathbf{v})(\mathbf{B}\cdot\hat{\phi}) + h\sin i\cos(\theta-\Omega)(\mathbf{r}\cdot\mathbf{v})(\mathbf{B}\cdot\hat{\theta})\right] \tag{6}$$

The first term in Eq. (6) shows that changes in inclination are coupled to changes in orbital energy, especially for orbits that are near circular (where $\mathbf{r}\cdot\mathbf{v}$ goes to zero) or polar (where $\cos i$ goes to zero). This coupling does not rise from some fundamental relationship between energy change and inclination change, but rather from the particulars of the Lorentz force. The energy change is driven by the radial component of the magnetic field and the apparent velocity induced by the rotation of the field. The inclination change is generally driven by the radial component of the magnetic field and the in-track velocity of the spacecraft. These velocities, magnetic field components, and perturbation equations happen to line up such that they depend upon the same dynamic quantities in the same relationships.

An expression for the change in eccentricity e is [14]

$$\dot{e} = \left[\frac{a}{\mu}(1-e^2)\right]^{1/2}\left\{(\mathbf{F}_\mathbf{L}\cdot\hat{\mathbf{r}})\sin\nu + [\mathbf{F}_\mathbf{L}\cdot(\hat{\mathbf{h}}\times\hat{\mathbf{r}})]\left(\cos\nu + \frac{e+\cos\nu}{1+e\cos\nu}\right)\right\} \tag{7}$$

This expression makes use of the Lorentz force $\mathbf{F}_\mathbf{L}$ explicitly.

Equations (3), (4), (6), and (7) are greatly simplified if we restrict our discussion to circular (or near circular) orbits, where the term $(\mathbf{r}\cdot\mathbf{v})$ vanishes. Applying this simplification to Eq. (3) yields

$$\dot{E} = \frac{q}{m}\omega_E\sqrt{\frac{\mu}{r^3}}\sin i\cos u(\mathbf{B}\cdot\hat{\mathbf{r}}) \tag{8}$$

The argument of latitude is defined as the angle from the point of right ascension of the ascending node (RAAN) to the spacecraft's position, measured around the orbit. Only the radial component of the magnetic field affects the orbital energy of a circular LAO. If the same simplification is applied to Eq. (4), we find that the change in scalar angular momentum is simply a multiple of the change in energy:

$$\dot{h} = \sqrt{\frac{r^3}{\mu}}\dot{E} \tag{9}$$

The inclination change in a circular orbit follows the same pattern:

$$\frac{\mathrm{d}i}{\mathrm{d}t} = \frac{\frac{\omega_E r^2}{h}\cos i - 1}{h\omega_E\sin i}\dot{E} \tag{10}$$

Equation (10) implies that, in circular orbits, orbital energy and inclination are not independently controllable with the Lorentz force. For every increase in energy, there is a corresponding decrease in inclination. (This fact also holds true for any polar orbit, eccentric or not.) This correlation limits the maneuvers that can be performed with LAO-based propulsion.

The circular-orbit assumption simplifies Eq. (7), resulting in

$$\dot{e} = \frac{q}{m}\frac{h}{\mu}\left\{2\frac{\omega_E}{h}\sqrt{\frac{a}{\mu}}r^2\sin i\cos(\theta-\Omega)\sin\phi\cos\nu(\mathbf{B}\cdot\hat{\mathbf{r}}) + \sin\nu\left(\omega_E r\sin\phi - \frac{h}{r}\frac{\cos i}{\sin\phi}\right)(\mathbf{B}\cdot\hat{\phi}) - \frac{h}{r}\sin i\cos(\theta-\Omega)\sin\nu(\mathbf{B}\cdot\hat{\theta})\right\} \tag{11}$$

The change in eccentricity depends on all three components of the magnetic field, making for more complicated analysis. Each term in Eq. (11) involves the true anomaly ν. This relationship shows the importance of radial velocity, which is also explicitly related to ν. Changes in eccentricity are driven by small deviations from the circular-orbit assumption.

III. Geomagnetic Field

The simplest model of the Earth's magnetic field is a dipole aligned with Earth's spin axis. However, this simple model fails to describe two important features for an LAO: that the dipole component is not aligned with the Earth's spin axis and that terms higher in degree than the dipole are significant components of the field. The Earth's magnetic field is best described as a full spherical-harmonic expansion [15]. Here, spherical-harmonic coefficients released as the International Geomagnetic Reference Field are used [16], in particular, the IGRF95 (or IGRF-7) model. All simulations in this study use coefficients up to 10th degree and order. An important note on the magnetic field is that it is represented in Earth-fixed coordinates. The field itself is locked in step with the rotation of the Earth [17]. One must be careful to distinguish between Earth-fixed longitudes and inertial longitudes.

The effect of the Lorentz force on an orbit is conveniently broken up into the components of the magnetic field in spherical-coordinate unit vectors: the radial direction $\hat{\mathbf{r}}$, the colatitude direction $\hat{\phi}$, and the azimuthal direction $\hat{\theta}$. The magnetic field $\mathbf{B}$ is studied as the three components $(\mathbf{B}\cdot\hat{\mathbf{r}})$, $(\mathbf{B}\cdot\hat{\phi})$, and $(\mathbf{B}\cdot\hat{\theta})$. Figure 2 shows a contour plot of $(\mathbf{B}\cdot\hat{\mathbf{r}})$ over (Earth-fixed) latitude and longitude at an altitude of 600 km. Positive values are represented by dotted gray contours, and negative contours are dashed gray. The black contour is referred to as the magnetic equator and indicates where the radial component is zero. In the traditional lexicon, the magnetic equator is where the field has no inclination (or "dip"). For an axis-aligned dipole model, the magnetic equator would lie on the latitudinal equator, but the additional higher-degree terms modify its location significantly.

Figure 3 shows a contour plot of $(\mathbf{B}\cdot\hat{\phi})$. Again, dashed gray contours are negative and dotted gray positive, with black being zero. The $\hat{\phi}$ component of the field is generally negative, except for small polar regions. The $\hat{\phi}$ component is small near these polar regions and is largest near the magnetic equator.

Figure 4 shows a contour plot of $(\mathbf{B}\cdot\hat{\theta})$. The contour colors are as previously described. Figure 4 shows distinct regions of positive and negative values. The zero contour represents the line of zero declination (or zero difference between true north and magnetic north). The dipole component of the field (and all other zero-order terms) contributes nothing to the $\hat{\theta}$ component of the field.

The three orthogonal components of the field can be used to divide the space of latitude and longitude into eight distinct zones. The zones are defined by whether each component is positive or negative and are bounded by the zero contours depicted in Figs. 2–4. The zones are numbered I–VIII and are depicted graphically in Fig. 5 with properties shown in Table 1. Figure 5 shows each of the zones superimposed on a map of the Earth. Because of distortion due to the map projection, zones I, II, VII, and VIII are shown larger than their actual sizes. In a three-dimensional view, they appear in a small region near each pole. The large southward swing of the zero-declination contour over eastern Africa actually crosses the magnetic equator, causing zones III and V to have noncontiguous regions. Table 1 lists the differences among the zones. A '+' in the table refers to a quantity greater than zero, and a '−' denotes less than zero.

In each zone, the geomagnetic field has a certain sign for a particular component of the field. Each zone creates different effects on the orbit of a charged satellite. We use these differences to create a control sequence to perform a desired maneuver. The zones are defined with respect Earth-fixed latitude and longitude as the geomagnetic field rotates with the Earth. Figures 2–4 are for a representative altitude (600 km) because the relative strength of each order of field terms depends on this altitude. Although the actual zone boundaries depend on altitude, they are easily calculated at any particular location by the simple sign definitions shown in Table 1.

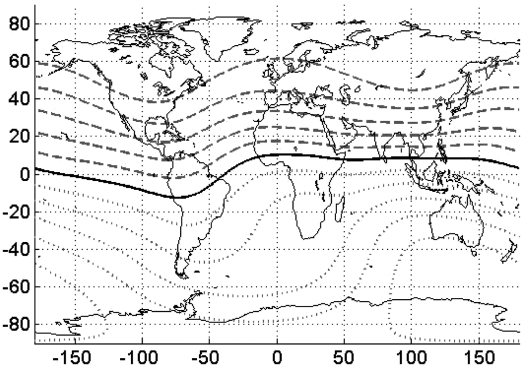

Fig. 2 Contour plot of the radial component of the geomagnetic field over latitude and longitude.

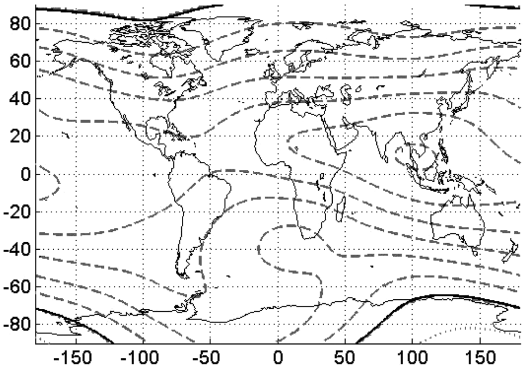

Fig. 3 Contour plot of the component of the geomagnetic field in the $\hat{\phi}$ direction over latitude and longitude.

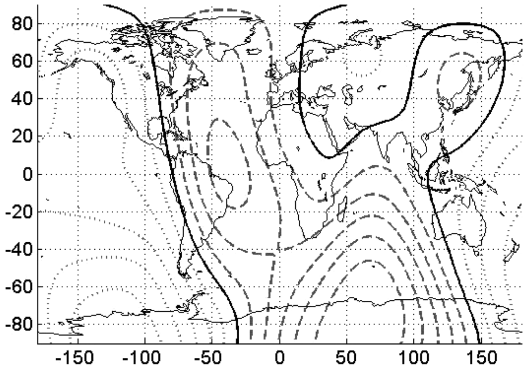

Fig. 4 Contour plot of the component of the geomagnetic field in the $\hat{\theta}$ direction over latitude and longitude.

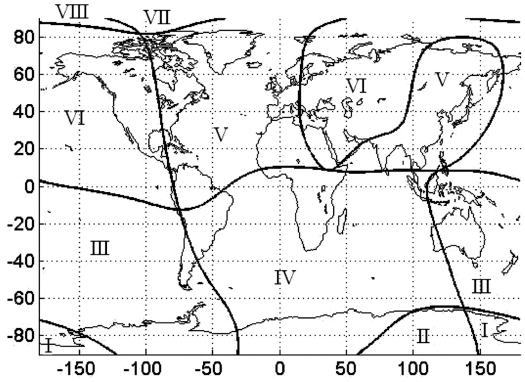

Fig. 5 Eight distinct zones of the geomagnetic field, numbered I–VIII.

Table 1 Zone properties

Zone	$(\mathbf{B}\cdot\hat{\mathbf{r}})$	$(\mathbf{B}\cdot\hat{\phi})$	$(\mathbf{B}\cdot\hat{\theta})$
I	+	+	+
II	+	+	−
III	+	−	+
IV	+	−	−
V	−	−	−
VI	−	−	+
VII	−	+	−
VIII	−	+	+

IV. Space-Vehicle Design

This section offers a brief overview of possible architectures for LAO capable spacecraft. It considers three competing, interrelated parameters: capacitance, power, and space-vehicle mass. There are also issues of implementation, such as deployability of the capacitor, technology readiness of the power system, thermal implications of high power, and interactions among various subsystems (notably attitude control). These issues are minimized here. For the present, maximizing the q/m metric is taken to be the only goal of LAO space-vehicle design. Furthermore, we consider this metric only in terms of a constant-mass spacecraft. Six hundred kilograms is chosen as a somewhat arbitrary constraint for this mass optimization. The mass is given some contingency.

A. Capacitance

High q/m implies high charge, which requires high capacitance. Known technologies for self-capacitance store charge on the surface of a conductor with no sharp local features or high curvature. So, a successful design realizes high surface area to volume in flat structures or long, thin ones. Such a capacitor likely encounters a limit associated with the minimum thickness of thin films or the minimum feasible diameter of long filaments. That limit ultimately leads to a minimum mass for the capacitor. The capacitor is also designed to exploit plasma interactions. Based on work by Choinière and Gilchrist [18], we have baselined a cylindrical capacitor constructed of a sparse wire mesh. This stockinglike arrangement of appropriately spaced thin wires develops a plasma sheath due to ionospheric interactions that raises the capacitance of the cylinder well above what it would be in a pure vacuum. We emphasize that such self-capacitance is not available from off-the-shelf electronics components, which merely hold equal amounts of positive and negative charge.

In this model, the capacitance C is taken to be that of a solid cylinder of the stocking's radius R but with a concentric shell (due to the plasma sheath) equal to the thickness of an individual wire's sheath r_s:

$$C = \frac{2\pi\epsilon_0 L}{\log\frac{R+r_s}{R}} \tag{12}$$

where ϵ_0 is the permittivity of free space. The sheath radius increases with potential and is calculated as described by Choinière and Gilchrist [18]. In the architecture described in Sec. IV.B, R takes on values of tens to hundreds of meters. The sheath thickness r_s depends on the temperature and density of the plasma and on capacitor potential, ranging from millimeters to meters in earth orbit. We space these wires so that one wire is a sheath's thickness away from its neighbor. This spacing ensures overlap between individual wires' sheaths but keeps the structure sparse. Occasional structural elements, such as thin conductive bands, would be necessary to maintain the spacing along the capacitor because of coulomb repulsion that acts among the wires. This repulsion would also serve as a useful means for deploying the capacitor without heavy trusses or actuators. A schematic of this design is shown in Fig. 6.

B. Power

We consider two fundamentally different approaches to the power subsystem. The classical approach depends on solar power. Energy from solar panels is used directly to power the capacitor, countering the plasma currents, or is stored in batteries or some sort of efficient ultracapacitor to be used in a periodic-charging scheme. Some assumptions about the specific power (W/kg) must be made. Although the power density of current systems is about 40 W/kg [19], a farther-term power density of 130 W/kg, is used here, consistent with DARPA's Fast Access Spacecraft Testbed (FAST) program [20].

In the case of this solar-power approach, the charge is maintained by modifying the current collection scheme proposed by Sanmartin et al. [21]. A power supply onboard the spacecraft establishes a potential between two conductive surfaces exposed to the plasma environment. The positive end attracts the highly mobile electrons, while the negative end attracts the far less mobile ions (such as O^+). The substantial imbalance in electron and ion currents leads the negative end to accumulate a nonzero charge while the positive end is almost electrically grounded in the plasma. So, with the wire capacitor on the negative end, the spacecraft would achieve a net charge roughly equal to the product of the capacitance of the wires and the potential across the power supply [18]. This charge is accomplished without the use of particle beams.

A more unusual approach exploits alpha-particle emission from an appropriate radioactive isotope [22], such as Po 210. These emissions are not converted to electrical power thermionically as in a radioisotope thermoelectric generator or via fission in a nuclear reactor; instead, the isotope is spread thinly enough on the capacitor's surface that up to half of the emitted alpha particles carry charge away from the spacecraft. The electrical current of these particles is proportional to their charge (two positive fundamental charges), their kinetic energy (roughly 5.3×10^6 eV), and the isotope's decay rate. If the maximum potential can be achieved despite currents from the surrounding ionospheric plasma, this approach offers as much as 42 kW/kg of Po 210 after one year of alpha decay. Maintaining this charge requires no power supply. The spatially distributed nature of the current from the thin film suggests that the current does not approach any sort of beam-density limit due to space charge.

We focus on the prospects for the solar-panel approach because launching an isotope is likely to encounter a variety of technical and nontechnical roadblocks. In all cases, the capacitor maintains negative charge. The ion currents are then given by the orbit motion limited estimate [18]. We use the International Reference Ionosphere (IRI) [23] to provide the necessary plasma number density and temperature. We also account for the photoelectric current emitted from the surface of the conductive capacitor. In the case of the solar-panel approach, all of this power is subject to resistive losses as the power supply drives current through the many thin wires. Assuming that the current is uniform to all parts of the capacitor, we average the losses along the length of wire that the current has to travel.

C. Space-Vehicle Mass

The charge-to-mass ratio depends on the mass of the entire space vehicle. We model this mass coarsely, as the sum of discrete

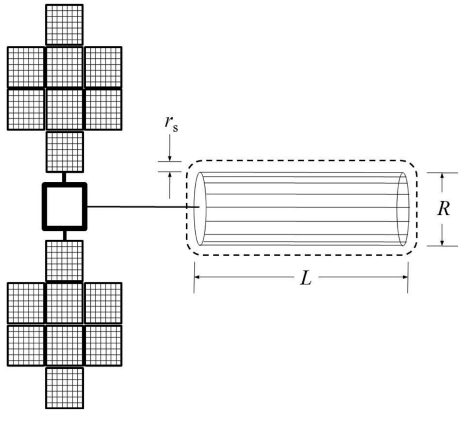

Fig. 6 LAO spacecraft with cylindrical stocking capacitor.

Table 2 Space-vehicle mass model

Subsystem or component	Value	Units
Payload	50	kg
Bus (w/ payload power)	3.33	(kg bus)/(kg payload)
LAO solar power	130	W/kg of orbit-average power
LAO isotope power	42	kW/kg of polonium after 1 yr of decay
Power mass contingency	14	kg
Capacitor	$2700\pi R^2 nL$	kg for n aluminum wires of length L and radius R
Capacitor mass contingency	$1.1m$	kg, where m is the sum of the wires' masses

components with interrelated dependencies. Table 2 summarizes this mass model.

An example of the power calculation is shown in Table 3. Table 4 uses this power calculation to arrive at the 600 kg space-vehicle mass requirement.

D. Performance Estimates

Figure 7 summarize the results of these calculations for a 600 kg spacecraft that charges for 50% of the time over a 600 km orbit. Figure 7 shows the FAST power design, which yields $q/m = 0.0070$ C/kg for a 20 km stocking at 7 kV potential. The efficiency (force per power) increases with lower potential. For example, the optimal value of $5C$ in a 600 km polar orbit produces about 2.3 N, for 1.6×10^{-5} N/H when the capacitor is charged. However, at only 1 kV, the resulting $3.1C$ represents 2×10^{-5} N/W. So, if the speed of the maneuver is unimportant, lower-potential designs may be better. As the capacitor potential increases beyond the optimum for q/m, more mass of the fixed 600 kg must be devoted to the power subsystem, which comes at the expense of capacitor mass. The accuracy of these performance measures depends on the accuracy of the simplified sheath model and should eventually be verified by a more complex 2-D algorithm such as that developed by Choinière and Gilchrist [18].

Table 3 Example of power calculation for a spacecraft in a 600 km altitude LEO circular orbit at an inclination of 28.5 deg

Parameter	Value	Units
Wire material	Aluminum	
Wire radius	5.00×10^{-6}	m
% overlap sheath diameter	0%	
Length of stocking, L	20	km
Stocking radius as a % of stocking length	5.00%	
Stocking mass sandbag	3	kg
Intermediate calculation	*Value*	*Units*
Material resistivity at 20°C	2.82×10^{-8}	Ω
Radius of stocking, R	1	km
Material density of wire	2700	kg/m^3
Sheath thickness	1.764	m
Resistance per wire	7.198	MΩ
Number of wires	7142	
Mass of stocking	30.36	kg
Mass of capacitor	33.40	kg
Average cylinder-as-body capacitance, C	6.00×10^{-4}	F
Result	*Value*	*Units*
Average body charge-to-mass ratio	−0.0070	C/kg
Exposed wire area	2548	m^2
Photoelectron current	0.122	A
Orbit-average power required (∼50% duty cycle)	53.54	kW

Table 4 Example of mass calculation

Parameter	Value	Units
Potential	−7000	V
Orbit-average power for LAO	46.28	kW
LAO power system mass dependency	130	W/kg
LAO power system mass	466	kg
Power system mass contingency	14	kg
Payload	20	kg
Bus mass (including any propellant)	100	kg
Total space-vehicle mass	600	kg

V. Lorentz Augmented Orbit Maneuvers and Limitations

A. Maneuver Limitations

A Lorentz augmented orbit cannot experience arbitrary changes for all initial orbital elements. In certain regimes, as evidenced by Eq. (10), changes in orbital elements are tightly coupled. This coupling stems from the basic physics of the Lorentz force. The direction of the force is set by the magnetic field and the velocity of the spacecraft with respect to that magnetic field, neither of which can be altered by the spacecraft control system.

A further limiting factor is that the best system architectures provide only one polarity of charge (negative). Because electrons in the ionosphere are far more mobile than ions, significantly less power is required to maintain a negative charge than a positive charge. The single-polarity system limits what changes can be made to the RAAN Ω and the argument of perigee ω. For a given charge polarity, Ω and ω evolve only in a single direction (in low Earth orbit). For a negative charge in LEO, Ω always decreases and ω always increases.

Table 5 summarizes some of the abilities and limits of LAO for a single polarity of charge. The first column of the table shows the net effect of a constant charge on a spacecraft. The second column shows the available directions of change for each orbital element for a variable (but single polarity) charge. The final column summarizes some the special cases and coupling within the dynamics. Some of these special cases are addressed more explicitly in our earlier work [2,3].

The Lorentz force is at its strongest in LEO. The strength of the dipole component of the magnetic field drops off with the cube of radial distance. Additionally, spacecraft velocities with respect to the magnetic field tend to be larger in LEO. A geostationary spacecraft has no velocity with respect to the magnetic field and thus experiences no Lorentz force.

B. Example Maneuver: Low-Earth-Orbit Inclination Change and Orbit Raising

The minimum inclination a spacecraft can be launched into is equal to the latitude of its launch site. For a United States launch, this minimum inclination is generally 28.5 deg, the latitude of Cape Canaveral, FL. However, for certain missions, equatorial orbits are desirable. The plane change between $i = 28.5$ deg and $i = 0$ deg is expensive in terms of ΔV and requires either a launch vehicle upper stage or a significant expenditure of spacecraft resources. We develop a control algorithm to use the Lorentz force to perform this inclination change without the use of propellant, while simultaneously raising the orbital altitude.

This maneuver is primarily concerned with inclination change in circular orbit. Equation (10) describes the relevant dynamics. As energy change and inclination change are coupled in this situation, Eq. (8) describes both the energy and plane changes. In this circular case, only the radial component of the magnetic field affects the energy and inclination. For the inclination to decrease, the energy must increase. With these facts, we develop a bang-off controller based upon the argument of latitude and the sign of the radial component of the field. Using $q/m < 0$, the term $\cos u(\mathbf{B} \cdot \hat{\mathbf{r}})$ must be

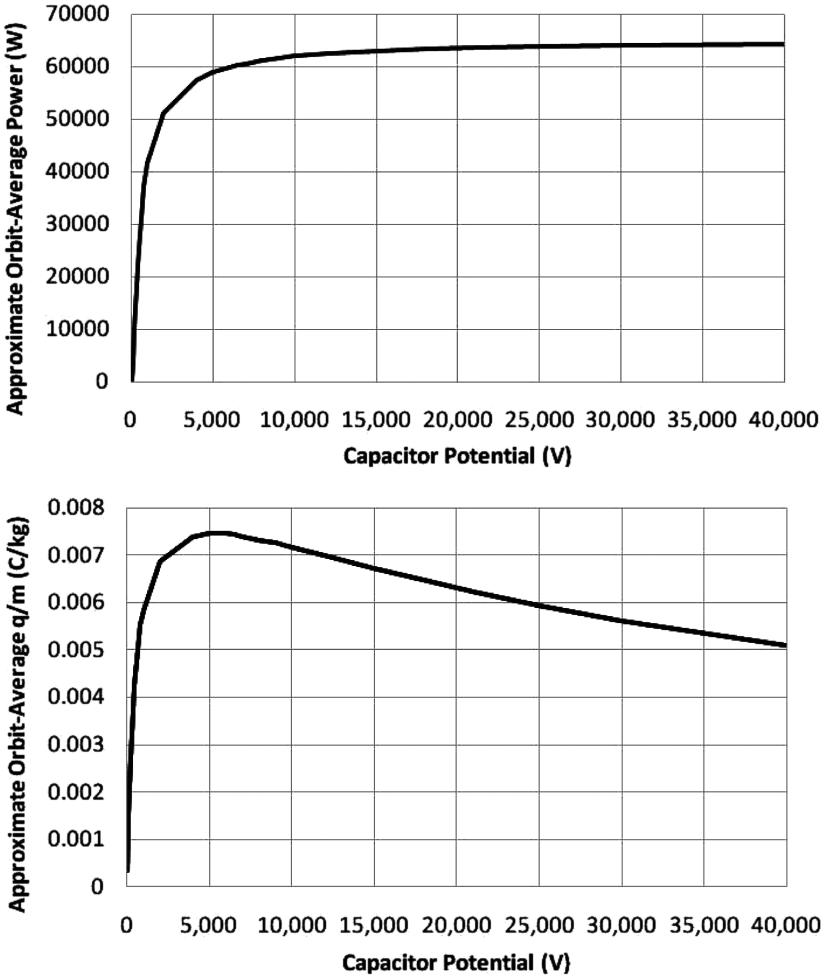

Fig. 7 Orbit-average power and q/m vs capacitor potential.

negative. We know that $(\mathbf{B}\cdot\hat{\mathbf{r}})$ is positive below the magnetic equator (zones I, II, III, and IV) and negative above the magnetic equator (zones V, VI, VII, and VIII). Thus, for northward motion of the satellite ($\cos u > 0$), the charge should be nonzero within zones V–VIII. For southward satellite motion ($\cos u < 0$), nonzero charge is applied in zones I–IV. In other words, the charge should be off for the first quadrant of the orbit, on for the second quadrant, off for the third, and on for the fourth. This control can be represented as

$$\frac{q}{m} = \begin{cases} -(\frac{q}{m})_{\max} & \text{if } \cos u > 0, (\mathbf{B}\cdot\hat{\mathbf{r}}) < 0 \\ 0 & \text{if } \cos u > 0, (\mathbf{B}\cdot\hat{\mathbf{r}}) > 0 \\ -(\frac{q}{m})_{\max} & \text{if } \cos u < 0, (\mathbf{B}\cdot\hat{\mathbf{r}}) > 0 \\ 0 & \text{if } \cos u < 0, (\mathbf{B}\cdot\hat{\mathbf{r}}) < 0 \end{cases} \tag{13}$$

where $-(q/m)_{\max}$ is largest available negative charge-to-mass ratio.

However, when this simple quadrant control is used, the eccentricity of the orbit tends to grow undesirably large. Maintaining an identically zero eccentricity is impossible, though. Any charge on a circular-orbiting spacecraft causes an increase in the eccentricity. However, if the oblateness of the Earth is considered, the eccentricity remains bounded by a small value. Figure 8 shows this result, plotting a short simulation of an orbit under the quadrant controller. The black line shows the growth of eccentricity with J2 absent, while the gray line shows the bounding of e under the influence of J2. The effect of J2 on the eccentricity of the orbit is larger than that of the Lorentz force. The J2 perturbation does not effect the overall performance of the maneuver, though. The Lorentz force depends on the velocity of the spacecraft which only changes by small amount due to presence of J2. The presence of J2 only creates a small periodic disturbance to both a and e.

Table 5 LAO effects for $q/m < 0$ in LEO

Element	Net effect of constant charge	Signs of possible changes	Notes
a	0	$\pm$	a/i coupled for $e = 0$ or $i = 90$ deg, $\dot{a} = 0$ for $i = 0$ deg and $e = 0$
e	0	$\pm$	$\dot{e} > 0$ for $e = 0$
i	0	$\pm$	a/i coupled for $e = 0$ or $i = 90$ deg
Ω	$-$	$-$	Ω undefined for $i = 0$ deg
ω	$+$	$+$	ω undefined for $i = 0$ deg and $e = 0$
ν	0	$\pm$	

Figure 9 shows the results of a simulation using the e-limiting quadrant method. The simulation begins with a 600 km altitude circular orbit. The charge-to-mass ratio is $q/m = -0.007$ C/kg. A full model of J2 is used. The simulation lasts until an equatorial orbit is reached. The IGRF95 magnetic field model is used to 10th degree and order. Figure 9a shows the increase in semimajor axis given by the quadrant method. The initial 600 km orbit is raised to a 724.0 km circular orbit, an increase of 124 km. Figure 9b shows the desired decrease in inclination. Because the magnetic equator does not align with the true equator, the inclination can be brought to exactly zero. Zero inclination is reached in about 340 days with this value of charge. Figure 9c shows the eccentricity. The eccentricity is bounded by the J2 perturbation to a small value. Finally, Fig. 9d shows the RAAN. For a negative q/m in LEO, the RAAN always decreases, however, in this simulation, the effect of J2 on RAAN dominates.

If the aforementioned simulated maneuver is performed using conventional impulsive thrust, it requires a ΔV of 3.75 km/s. Thus, using LAOs could significantly increase the payload ratio of a

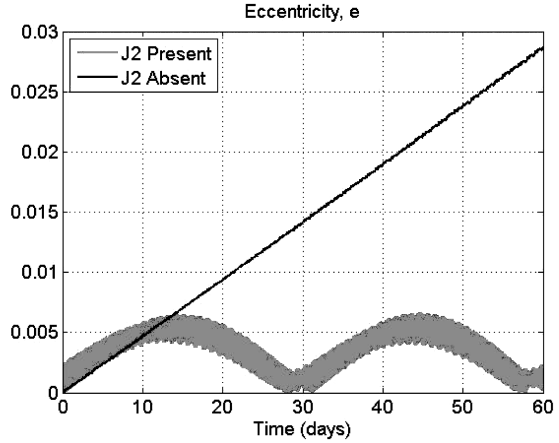

Fig. 8 Effect of Earth oblateness on the eccentricity under the quadrant control.

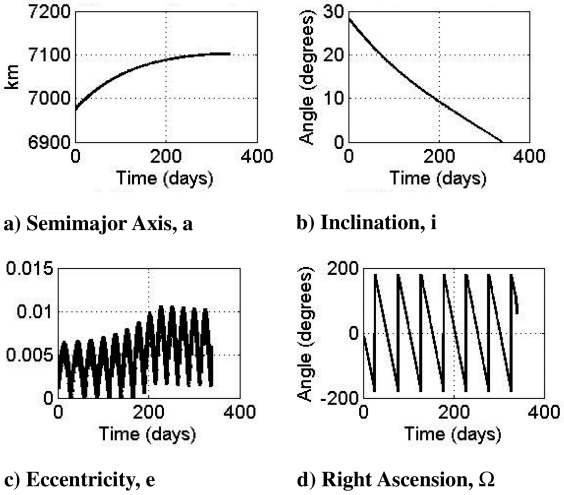

a) Semimajor Axis, a **b) Inclination, i**

c) Eccentricity, e **d) Right Ascension, Ω**

Fig. 9 Orbital elements for the LEO plane change and orbit-raising maneuver.

spacecraft that needed such a maneuver. However, this mass savings comes at a cost of time spent, the mass of the capacitor and power system, and electrical power consumed during the maneuver.

VI. Lorentz Augmented Orbit Power Consumption and Plasma-Density-Based Control

The preceding simulations use a code that does not include a model of the Earth's ionosphere. The spacecraft design process is carried out initially using the IRI model, and then that design is used in simulation. The simulation assumes the spacecraft maintains its design charge-to-mass ratio, regardless of the local plasma conditions. In this section, we explore the use of a more in-depth LAO simulation by revisiting the LEO inclination-change maneuver. This simulation uses a code that takes into account local ionospheric conditions and their effect on the instantaneous charge-to-mass ratio and power consumption of the spacecraft.

The high-fidelity, plasmadynamics simulation is based upon the Global Core Plasma Model (GCPM) [24]. The GCPM model is a framework for blending multiple empirical plasma-density models and extending the IRI model to full global coverage. For the next simulations, the GCPM model at one particular time is used. This time corresponds to mean solar conditions. Although there is a strong correlation between plasma conditions and time of day, this effect is averaged out by simulating over the course of multiple days.

This simulation functions in a different fashion from the results presented in Sec. V. The earlier simulations assume that q/m is either zero or constant at a value of -0.007 C/kg. The GCPM simulation assumes that the spacecraft maintains a constant potential on the capacitor. Because of local variations in plasma density, a constant potential results in varying values of charge-to-mass ratio and varying power required to hold the constant potential. Although the mean q/m and orbit-average power are consistent with those predicted in our earlier analysis in Sec. IV, they have peak and minimum values that depend on the local plasma environment.

The local electron number density n_e is a strong predictor of power usage and is readily available from the GCPM model. A higher n_e corresponds to a denser plasma, which, in turn, results in more current collection for a stocking at a given potential. Thus, high-n_e values correlate to high power usage. In a gross sense, n_e is larger in the low- to midlatitudes on the daytime side of the Earth. The density of the plasma also drops sharply as a function of altitude.

Assuming the spacecraft has knowledge of its local plasma conditions, significant power savings can be realized by limiting the charge-on time when n_e is high. The spacecraft simply follows its normal control law but turns off the charge whenever n_e exceeds a particular value. A sample of this power savings and cost in time is shown in Table 6. This table lists the results of four simulations performed with the constant-potential code. Each simulation integrates over three days and begins with the same initial conditions. Reported for each run is the mean q/m achieved (during times of nonzero charging), the average power used (over the entire simulation), the peak instantaneous power used, the total inclination change over the simulation, and an efficiency in the form of degrees of inclination change per day divided by the average power used. The first simulation uses the e-limiting quadrant controller discussed earlier with no modification based on electron density. The other three runs superimpose an n_e-based, density-limited control, turning off the charge when n_e is greater than some value.

The average q/m achieved by each successive simulation is slightly lower, as seen in the first row of Table 6. In regions of high plasma density, the capacitance of the stocking is increased by a tighter plasma sheath, leading to a larger capacitance. However, this increase in q/m requires significantly more power to maintain, as the denser plasma greatly increases the current collected by the stocking. The power reduction due to density-limited control is shown in the second and third rows of Table 6. Without density-based control, the average power usage over the simulation is 53.54 kW, but with a peak instantaneous power usage of 418.57 kW. When charge is only applied for an n_e of less than 1.1×10^{11} m^{-3} (the mean electron density in this orbit), the power usage drops to a mean of 12.94 kW, with a peak of 89.59 kW. Of course, the decreased power usage is coupled with a lengthening of the maneuver time. Row 4 of Table 6 shows the inclination change achieved over three days for each level of density control. The unlimited control changes inclination at a rate about 2.2 times higher than the $n_e < 1.1 \times 10^{11}$ case. However, the density-limited controllers achieve inclination changes in a more

Table 6 Limiting power usage via n_e (in m^{-3}) sensing for three-day simulations at an initial inclination of $i = 28.5$ deg at an altitude of 600 km

	No n_e control	$n_e < 2 \times 10^{11}$	$n_e < 1.5 \times 10^{11}$	$n_e < 1.1 \times 10^{11}$
$(q/m)_{\text{mean}}$, C/kg	−0.0060	−0.0057	−0.0054	−0.0048
P_{mean}, kW	53.54	35.88	24.33	12.94
P_{peak}, kW	418.57	220.01	140.64	89.59
Δi, deg	0.3764	0.3292	0.2653	0.1747
deg /day/kW$_{\text{mean}}$	0.0023	0.0031	0.0036	0.0045

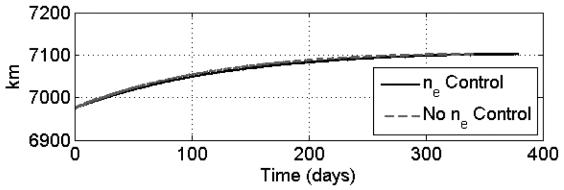

a) Semimajor axis, a

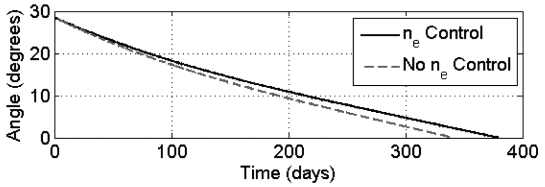

b) Inclination, i

Fig. 10 Comparison of hybrid simulation of constant charge-to-mass ratio with plasma-density-limited control to constant q/m-only control.

efficient way. The fifth row of Table 6 displays an efficiency metric for each simulation, namely degrees of inclination change achieved per day per average kilowatt used. Charging only at low values of n_e more efficiently uses the available power to effect inclination change.

The profile of electron densities experienced by a spacecraft varies greatly depending on its orbit. In the 28.5 deg inclination-change example, both the change in inclination and the change in altitude during the maneuver cause no one limit on n_e to be appropriate. However, recreating this entire maneuver using the GCPM, constant voltage simulation is impractical in its computational demands. A reasonable approximation is a hybrid simulation in which a constant charge-to-mass ratio is used, but the electron density is calculated at each step in the integration to superimpose the density-limited control strategy. To take advantage of the orbit raising that occurs during the maneuver, the n_e cutoff value is made a linear function of the spacecraft altitude. This line is defined by two points: n_e equal to 2.0×10^{11} m^{-3} at an altitude of 600 km, and n_e equal to 1.6×10^{11} m^{-3} at an altitude of 700 km. These values are chosen to give a reasonable tradeoff between power savings and maneuver time.

Figure 10 shows the results of this hybrid simulation. The top plot of this figure shows semimajor axis, while the lower plot gives the inclination, both versus time in days. The solid black lines are the results of the hybrid constant q/m, density-limited simulation. For comparison, the dashed gray lines show the results of the constant-charge-only simulation. The hybrid strategy completes the inclination-change maneuver in 380 days compared to 340 days for the original strategy.

To provide insight into the power saved by using the density-limited hybrid strategy, short-duration simulations are run using the full GCPM, constant voltage code. These simulations are run for three points in the trajectory of both the hybrid simulation and the original inclination-change maneuver. When each trajectory reaches 28.5, 10, and 1 deg of orbital inclination, its state is retrieved and used as the initial conditions for a three-day simulation using the full GCPM code. The results of these simulations are summarized in Table 7. This table gives the mean achieved charge-to-mass ratio, average and peak power consumptions, and inclination change over the three-day simulation for each control strategy for each inclination considered. The addition of density-limited control reduces both the mean and peak power usage but also decreases the speed of the inclination change.

Table 7 Comparison of power usage during both the hybrid simulation and the original, constant charge simulation

Inclination		Constant charge	Hybrid, density-limited
28.5 deg	$(q/m)_{\text{mean}}$, C/kg	−0.0060	−0.0057
	$P_{\text{mean}}(P_{\text{peak}})$, kW	53.54 (418.57)	36.50 (217.15)
	Δi, deg	0.3764	0.3308
10 deg	$(q/m)_{\text{mean}}$, C/kg	−0.0055	−0.0053
	$P_{\text{mean}}(P_{\text{peak}})$, kW	56.79 (259.47)	43.64 (208.58)
	Δi, deg	0.1806	0.1622
1 deg	$(q/m)_{\text{mean}}$, C/kg	−0.0055	−0.0053
	$P_{\text{mean}}(P_{\text{peak}})$, kW	58.39 (235.89)	43.54 (208.39)
	Δi, deg	0.1447	0.1330

VII. Conclusions

Lorentz augmented orbits use the Earth's magnetic field to provide propellantless propulsion. Although the direction of the Lorentz force is fixed by the velocity of the spacecraft and the local field, varying the magnitude of the charge-to-mass ratio of the satellite can produce novel and useful changes to an orbit. A simple on–off (or bang-off) charging scheme is sufficient to perform most available maneuvers and can create large savings of ΔV.

A preliminary evaluation of some possible architectures leads us to the tentative conclusion that up to 0.0070 C/kg can be reached by a negatively charged LEO spacecraft of 600 kg mass. These designs use cylindrical mesh "stocking" capacitive structures that are shorter than most proposed electrodynamic tethers and offer the important benefit that their performance is independent of their attitude in the magnetic field. That simplicity largely decouples attitude control from propulsion, a consideration that can complicate the operation of tether-driven spacecraft.

The Earth's magnetic field is a complex structure. Accurate analytical expressions for orbital perturbations are difficult to obtain. The proposed control method accommodates this complexity by breaking the geomagnetic field into distinct zones based on its sign in three orthogonal directions, leading to eight zones. Within each zone, an LAO tends to evolve in certain directions for certain orbital elements. Understanding how the orbital evolution relates to the zone the spacecraft is in allows us to develop control strategies to execute complex maneuvers. A simple, but effective strategy is to operate a bang-off control scheme that switches only at zone boundaries. This scheme allows for the execution of a sample maneuver of an LEO plane change without the use of propellant, saving a ΔV of 3.75 km/s required for a conventional propulsive maneuver. However, this maneuver lasts for 340 days and requires about 53 kW of power on average. A controller that limits charging in response to local plasma-density measurements reduces this power requirement to an average of 40 kW but increases the maneuver time to 380 days.

References

[1] Peck, M. A., "Prospects and Challenges for Lorentz-Augmented Orbits," *Proceedings of the AIAA Guidance, Navigation, and Control Conference*, AIAA Paper 2005-5995, Aug. 2005.

[2] Streetman, B., and Peck, M. A., "New Synchronous Orbits Using the Geomagnetic Lorentz Force," *Journal of Guidance, Control, and Dynamics*, Vol. 30, No. 6, 2007, pp. 1677–1690. doi:10.2514/1.29080

[3] Streetman, B., and Peck, M. A., "Gravity-Assist Maneuvers Augmented by the Lorentz Force," *Proceedings of the AIAA Guidance, Navigation, and Control Conference*, AIAA Paper 2007-6846, Aug. 2007.

[4] Schaffer, L., and Burns, J. A., "The Dynamics of Weakly Charged Dust: Motion Through Jupiter's Gravitational and Magnetic Fields," *Journal of Geophysical Research*, Vol. 92, No. A3, 1987, pp. 2264–2280. doi:10.1029/JA092iA03p02264

[5] Schaffer, L., and Burns, J. A., "Charged Dust in Planetary Magnetospheres: Hamiltonian Dynamics and Numerical Simulations for Highly Charged Grains," *Journal of Geophysical Research*, Vol. 99, No. A9, 1994, pp. 17211–17223. doi:10.1029/94JA01231

[6] Hamilton, D. P., "Motion of Dust in a Planetary Magnetosphere: Orbit-Averaged Equations for Oblateness, Electromagnetic, and Radiation Forces with Applications to Saturn's F Ring," *Icarus*, Vol. 101, No. 2, Feb. 1993, pp. 244–264 doi:10.1006/icar.1993.1022; Erratum: *Icarus* Vol. 103, p. 161.

[7] Sehnal, L., "The Motion of a Charged Satellite in the Earth's Magnetic Field," Smithsonian Inst. Tech. Rept., Smithsonian Astrophyiscal Observatory Special Rept. No. 271, June 1969.

[8] Vokrouhlicky, D., "The Geomagnetic Effects on the Motion of Electrically Charged Artificial Satellite," *Celestial Mechanics and Dynamical Astronomy*, Vol. 46, 1989, pp. 85–104. doi:10.1007/BF02426715

[9] Abdel-Aziz, Y., "Lorentz Force Effects on the Orbit of a Charged Artificial Satellite: A New Approach," *Applied Mathematical Sciences* [online], Vol. 1, Nos. 29–32, 2007, pp. 1511–1518, http://www.m-hikari.com/ams/ams-password-2007/ams-password29-32-2007/index.html.

[10] Cosmo, M. L., and Lorenzini, E. C., *Tethers in Space Handbook*, 3rd ed., NASA Marshall Spaceflight Center, Huntsville, AL, 1997, pp. 119–151.

[11] King, L. B., Parker, G. G., Deshmukh, S., and Chong, J., "A Study of Inter-Spacecraft Coulomb Forces and Implications for Formation Flying," *Journal of Propulsion and Power*, Vol. 19, No. 3, 2003, pp. 497–505. doi:10.2514/2.6133

[12] Schaub, H., Parker, G. G., and King, L. B., "Challenges and Prospects of Coulomb Spacecraft Formations," *Proceedings of the AAS John L. Junkins Symposium*, American Astronautical Society Paper 03-278, May 2003.

[13] Peck, M. A., Streetman, B., Saaj, C. M., and Lappas, V., "Spacecraft Formation Flying Using Lorentz Forces," *Journal of the British Interplanetary Society*, Vol. 60, July 2007, pp. 263–267, http://www.bis-spaceflight.com/sitesia.aspx/page/358/id/1444/l/en-us.

[14] Burns, J. A., "Elementary Derivation of the Perturbation Equations of Celestial Mechanics," *American Journal of Physics*, Vol. 44, No. 10, 1976, pp. 944–949. doi:10.1119/1.10237

[15] Roithmayr, C. M., "Contributions of Spherical Harmonics to Magnetic and Gravitational Fields," NASA, TR TM-2004-213007, March 2004.

[16] Barton, C. E., "International Geomagnetic Reference Field: The Seventh Generation," *Journal of Geomagnetism and Geoelectricity*, Vol. 49, Nos. 2–3, 1997, pp. 123–148.

[17] Rothwell, P. L., "The Superposition of Rotating and Stationary Magnetic Sources: Implications for the Auroral Region," *Physics of Plasmas*, Vol. 10, No. 7, 2003, pp. 2971–2977. doi:10.1063/1.1582473

[18] Choinière, E., and Gilchrist, B. E., "Self-Consistent 2-D Kinetic Simulations of High-Voltage Plasma Sheaths Surrounding Ion-Attracting Conductive Cylinders in Flowing Plasmas," *IEEE Transactions on Plasma Science*, Vol. 35, No. 1, 2007, pp. 7–22. doi:10.1109/TPS.2006.889300

[19] Wertz, J. R., and Larson, W. J., *Space Mission Analysis and Design*, Microcosm Press, El Segundo, CA, 1999, pp. 141–156.

[20] Fast Access Spacecraft Testbed (FAST), Defense Advanced Research Projects Agency Broad Agency Announcement, BAA-07-65, Nov. 2007.

[21] Sanmartin, J. R., Martinez-Sanchez, M., and Ahedo, E., "Bare Wire Anodes for Electrodynamic Tethers," *Journal of Propulsion and Power*, Vol. 9, June 1993, pp. 353–360. doi:10.2514/3.23629

[22] Linder, E. G., and Christian, S. M., "The Use of Radioactive Material for the Generation of High Voltage," *Journal of Applied Physics*, Vol. 23, No. 11, 1952, pp. 1213–1216. doi:10.1063/1.1702034

[23] Bilitza, D., "International Reference Ionosphere 2000," *Radio Science*, Vol. 36, No. 2, 2001, pp. 261–275. doi:10.1029/2000RS002432

[24] Gallagher, D. L., Craven, P. D., and Comfort, R. H., "Global Core Plasma Model," *Journal of Geophysical Research*, Vol. 105, No. A8, 2000, pp. 18,819–18,833. doi:10.1029/1999JA000241

D. Spencer
Associate Editor